

# Lawrence Berkeley National Laboratory

## LBL Publications

### Title

Imaging and quantification of spreading and trapping of carbon dioxide in saline aquifers using meter-scale laboratory experiments

### Permalink

<https://escholarship.org/uc/item/3fv5v9rr>

### Journal

Water Resources Research, 53(1)

### ISSN

0043-1397

### Authors

Trevisan, Luca

Pini, Ronny

Cihan, Abdullah

et al.

### Publication Date

2017

### DOI

10.1002/2016wr019749

Peer reviewed

1 **Imaging and quantification of spreading and trapping of carbon dioxide in saline aquifers**  
2 **using meter-scale laboratory experiments**

3 Luca Trevisan<sup>1,2</sup>, Ronny Pini<sup>3,4</sup>, Abdullah Cihan<sup>5</sup>, Jens T. Birkholzer<sup>5</sup>, Quanlin Zhou<sup>5</sup>, Ana  
4 Gonzalez-Nicolas<sup>1,5</sup>, Tissa H. Illangasekare<sup>1</sup>

5 <sup>1</sup>Center for Experimental Study of Subsurface Environmental Processes (CESEP), Department of  
6 Civil and Environmental Engineering, Colorado School of Mines, Golden, Colorado, USA

7 <sup>2</sup>Now at Gulf Coast Carbon Center, Bureau of Economic Geology, Jackson School of Geosciences,  
8 University of Texas at Austin, Austin, Texas, USA

9 <sup>3</sup>Department of Petroleum Engineering, Colorado School of Mines, Golden, Colorado, USA

10 <sup>4</sup>Now at Department of Chemical Engineering, Imperial College, London, UK

11 <sup>5</sup>Energy Geosciences Division, Lawrence Berkeley National Laboratory, University of California,  
12 Berkeley, California, USA

13 Corresponding author: Luca Trevisan ([luca.trevisan@gmail.com](mailto:luca.trevisan@gmail.com))

14

15        **Abstract**

16        The role of capillary forces during buoyant migration of CO<sub>2</sub> is critical towards plume  
17 immobilization within the post-injection phase of a geological carbon sequestration operation.  
18 However, the inherent heterogeneity of the subsurface makes it very challenging to evaluate the  
19 effects of capillary forces on the storage capacity of these formations and to assess in-situ plume  
20 evolution. To overcome the lack of accurate and continuous observations at the field scale and to  
21 mimic vertical migration and entrapment of realistic CO<sub>2</sub> plumes in the presence of a background  
22 hydraulic gradient, we conducted two unique long-term experiments in a 2.44 m × 0.5 m tank. X-  
23 ray attenuation allowed measuring the evolution of non-wetting phase (NWP) saturation, thus  
24 providing direct insight into capillarity- and buoyancy-dominated flow processes occurring under  
25 successive drainage and imbibition conditions. The comparison of saturation distributions between  
26 two experimental campaigns suggests that layered-type heterogeneity plays an important role on  
27 NWP migration and trapping, because it leads to (i) longer displacement times (3.6 months vs. 24  
28 days) to reach stable trapping conditions, (ii) limited vertical migration of the plume (with center  
29 of mass at 39% vs. 55% of aquifer thickness), and (iii) immobilization of a larger fraction of  
30 injected NWP mass (67.2% vs. 51.5% of injected volume) as compared to the homogenous  
31 scenario. While these observations confirm once more the role of geological heterogeneity in  
32 controlling buoyant flows in the subsurface, they also highlight the importance of characterizing  
33 it at scales that are below seismic resolution.

34        **Keywords:** surrogate fluids; sandbox experiments; migration and trapping; injection schemes;  
35 geological carbon storage

36

37 **Highlights:**

- 38 • We present a set of m-scale sandbox experiments designed to replicate field scale CO<sub>2</sub>  
39 injection configuration and contrast in fluid properties
- 40 • Multiple injection events, each followed by longer imbibition, are used to achieve larger  
41 plume footprints, higher trapping efficiency, and larger total mass trapped
- 42 • X-ray attenuation is used for accurate quantification of CO<sub>2</sub>-analog saturation and mass  
43 balance calculations
- 44 • Time scales associated with stabilization of the plume are greatly enhanced by  
45 heterogeneity

46

## 47 **1. Introduction**

48 Geological Carbon Storage (GCS) has the potential to stabilize and eventually reduce  
49 anthropogenic emissions of CO<sub>2</sub> to the atmosphere, thus facilitating the transition from fossil  
50 energy production to an extensive use of renewables. For GCS to considerably reduce global  
51 carbon emissions, large volumes of CO<sub>2</sub> have to be stored underground. This can be accomplished  
52 by taking advantage of the heterogeneous nature of deep brine-bearing sedimentary formations  
53 and by designing appropriate injection schemes. The heterogeneous nature of geological media  
54 plays a critical role in controlling the migration and entrapment of injected CO<sub>2</sub> by affecting the  
55 efficiency of both dissolution [*Agartan et al.*, 2015; *Farajzadeh et al.*, 2011] and capillary trapping  
56 [*Bryant et al.*, 2008; *Trevisan et al.*, 2015]. Hence, it becomes crucial to consider the influence of  
57 natural heterogeneity on storage capacity and efficiency whenever candidate reservoirs are  
58 identified [*Kopp et al.*, 2009]. Assuming that most candidate reservoirs are inherently  
59 heterogeneous, we can expect a persistent presence of so-called capillary barriers that possess  
60 variable spatial continuity and that lead to the plume concentrating in high permeability streaks  
61 and pooling behind less permeable layers. Because characterizing deep reservoirs' heterogeneity  
62 and assessing in-situ plume behavior (by means of e.g. preferential flow and fluid saturation  
63 evolution) is practically difficult, intermediate scale (dm-m) immiscible displacement experiments  
64 represent a convenient method for studying the influence of heterogeneity on macroscale migration  
65 and trapping phenomena. A further advantage of synthetic aquifers is the ability to test injection  
66 schemes that have potential applications in real storage scenarios. In the context of this work, we  
67 investigate the role of capillary forces during buoyant migration of CO<sub>2</sub> as a critical factor towards  
68 plume immobilization during post-injection of carbon storage in deep saline aquifers.

69 In general, the action of capillarity on immiscible fluid displacement manifests itself via two  
70 major phenomena, namely hysteresis and capillary barrier, causing occurrence of non-wetting  
71 phase (NWP) at different saturations across the porous medium. The importance of these  
72 phenomena has been pointed out by several numerical modeling studies focusing on a variety of  
73 specific aspects at the field scale [*Bryant et al.*, 2008; *Deng et al.*, 2012; *Doughty and Pruess*,  
74 2004; *Flett et al.*, 2007; *Saadatpoor et al.*, 2010] and at the sub-meter scale [*Kuo and Benson*,  
75 2015; *Li and Benson*, 2015; *Ritzi et al.*, 2016; *Trevisan et al.*, under review]. For example, spatial  
76 correlation of the permeability ( $k$ ) field as well as interconnectivity of high- $k$  preferential flow  
77 pathways have a critical impact on CO<sub>2</sub> migration and trapping in saline aquifers [*Gershenson et*  
78 *al.*, 2015; *Han et al.*, 2010; *Ide et al.*, 2007; *Lengler et al.*, 2010; *Tian et al.*, 2016]. The modeling  
79 approach has also been followed, either numerically [*Buscheck et al.*, 2012; *Gasda et al.*, 2008;  
80 *Goater et al.*, 2013; *Yamamoto et al.*, 2009] or analytically [*Gunn and Woods*, 2011; *Hesse et al.*,  
81 2006; *MacMinn et al.*, 2010; *Zimoch et al.*, 2011], to understand the behavior of a CO<sub>2</sub> plume in  
82 concomitance with regional groundwater flow and sloping caprock. Injection strategies aimed at  
83 enhancing the storage capacity and efficiency of saline formations have also been explored by  
84 means of numerical models [*Buscheck et al.*, 2012; *Cameron and Durlofsky*, 2012; *Cihan et al.*,  
85 2015; *Gonzalez-Nicolas et al.*, under review; *Huber et al.*, 2016; *Rasmusson et al.*, 2016].

86 While numerical simulations have shed light on the influence of some of the geological and  
87 engineering aspects that control CO<sub>2</sub> trapping mechanisms, validation by means of experiments is  
88 still lacking. Hereby, the difficulty in carrying out controlled field experiments has always  
89 involved uncertainty related to the rigorous application of boundary conditions and the exact  
90 distribution of sandstone rock types. Most of the work to date has focused on non-aqueous phase  
91 liquid (NAPL) migration observed in sandbox experiments [e.g. *Barth et al.*, 2003; *Fagerlund et*

92 *al.*, 2007; *Glass et al.*, 2000; *Kueper and Frind*, 1991], while studies that specifically address GCS  
93 are quite scarce and are limited to cm-to-m observations of immiscible [*Pini et al* 2012; *Polak et*  
94 *al.*, 2015; *Trevisan et al.*, 2014; *Werner et al.*, 2014; *Zhao et al.*, 2014] and miscible displacements  
95 [*Agartan et al.*, 2015; *Neufeld et al.*, 2010]. A dimensional analysis approach has also been  
96 proposed to reconcile laboratory- and field-scales [*Cinar et al.*, 2009; *Polak et al.*, 2015; *Trevisan*  
97 *et al.*, 2014; *Werner et al.*, 2014]. In this context, physical models prove to be very useful, because  
98 they enable a systematic evaluation of flow regimes and heterogeneity contrasts in terms of e.g.,  
99 strength and correlation length of a permeability field. However, while studies so far have  
100 integrated heterogeneity in a simplified fashion, it has been long recognized that the complex  
101 geometrical arrangement of typical sedimentary facies plays a major role in capillary trapping  
102 [*Mikes and Bruining*, 2006; *Pickup et al.*, 2000; *Ringrose et al.*, 1993; *van Lingen et al.*, 1996].

103 To address the lack of geological realism of prior experimental studies, as well as the limited  
104 dimensional size available for long-term observation of migration and trapping phenomena, a set  
105 of sandbox experiments is performed in this study on a larger (2.44 m × 0.5 m) system. The setup  
106 is unique as it enables introducing realistic subsurface conditions, thus including the presence of  
107 a) a background hydraulic gradient, b) significant buoyant forces, and c) a wider continuum of  
108 heterogeneity scale. Results from two experiments are presented that have performed with  
109 surrogate fluids at ambient pressure-temperature (*P-T*) conditions. The first experiment is  
110 conducted in a homogeneous configuration, while the second represents a more realistic  
111 heterogeneous scenario. The scope of this experimental analysis is twofold. On the one hand, we  
112 present a bench-scale demonstration of injection schemes controlling the migration and  
113 immobilization of a surrogate CO<sub>2</sub> plume with and without the influence of heterogeneity. On the  
114 other hand, we provide an explicit characterization of the permeability field and boundary

115 conditions, as well as quantification of fluid saturation distribution, for future comparison with  
116 continuum-based numerical simulations. The uniqueness of these experiments lies in the ability to  
117 reproduce and observe those large-scale phenomena that control plume migration while hinting at  
118 the time scale for immobilization involved with geological heterogeneity.

## 119 **2. Experimental approach and methods**

120 Two experiments are presented in this study: a homogeneous setup using #50 Granusil sand  
121 and a spatially correlated, facies-based heterogeneous scenario with equivalent geometric mean  
122  $\mu_{lnk}$  of  $3.86 \times 10^{-11}$  m<sup>2</sup> and a variance  $\sigma^2_{lnk}$  of 1.69. The two experiments presented in this study  
123 are carried out in a larger tank setup with respect to the studies by *Trevisan et al.* [2014] and  
124 *Trevisan et al.* [2015], offering the ability to recreate realistic plume spreading behavior through  
125 longer periods.

### 126 **2.1 Experimental fluids**

127 The experiments were conducted at ambient conditions with a pair of surrogate fluids that  
128 mimic the density and viscosity contrasts of scCO<sub>2</sub> and brine at reservoir *P-T* conditions, as  
129 reported in Table 1. However, these fluids are insoluble and do not allow for study of mixing and  
130 dissolution processes. Specifically, isoparaffinic oil (Soltrol 220) and a glycerol-water mixture  
131 (80:20 w/w) were chosen to represent the injected NWP and resident wetting-phase fluid (WP),  
132 respectively. Soltrol 220 was dyed red with Sudan IV (Fisher Scientific) and doped with 10% w/w  
133 Iodoheptane (Alfa Aesar) to allow for direct visualization of the fluid flow and to increase x-ray  
134 attenuation contrast between the two phases.

135 **Table 1** Summary of density ( $\rho$ ), viscosity ( $\mu$ ), and interfacial tension (IFT) of surrogate fluids  
136 at experimental *P-T* conditions and actual fluids of scCO<sub>2</sub> and brine at reservoir conditions.



phase	$\rho$ (kg/m <sup>3</sup> )	$\mu$ (mPa·s)	$\mu_{nw}/\mu_w$	$\rho_{nw}/\rho_w$	IFT (mN/m)
<b>Soltrol 220</b>	860	4.9			
<b>Glycerol-water</b>	1210	61	0.072	0.71	15
<b>scCO<sub>2</sub></b>	266-733 <sup>a</sup> (760 <sup>c</sup> )	0.023-0.0611 <sup>a</sup> (0.06 <sup>c</sup> )	0.026-0.20 <sup>a</sup> (0.075 <sup>c</sup> )	0.22-0.75 <sup>a</sup> (0.745 <sup>c</sup> )	19.8 <sup>b</sup>
<b>Brine</b>	945-1230 <sup>a</sup> (1020 <sup>c</sup> )	0.195-1.58 <sup>a</sup> (0.8 <sup>c</sup> )			

137 <sup>a</sup> estimates from *Nordbotten et al.* [2005], T = 35-155°C, P = 10.5-31.5 MPa

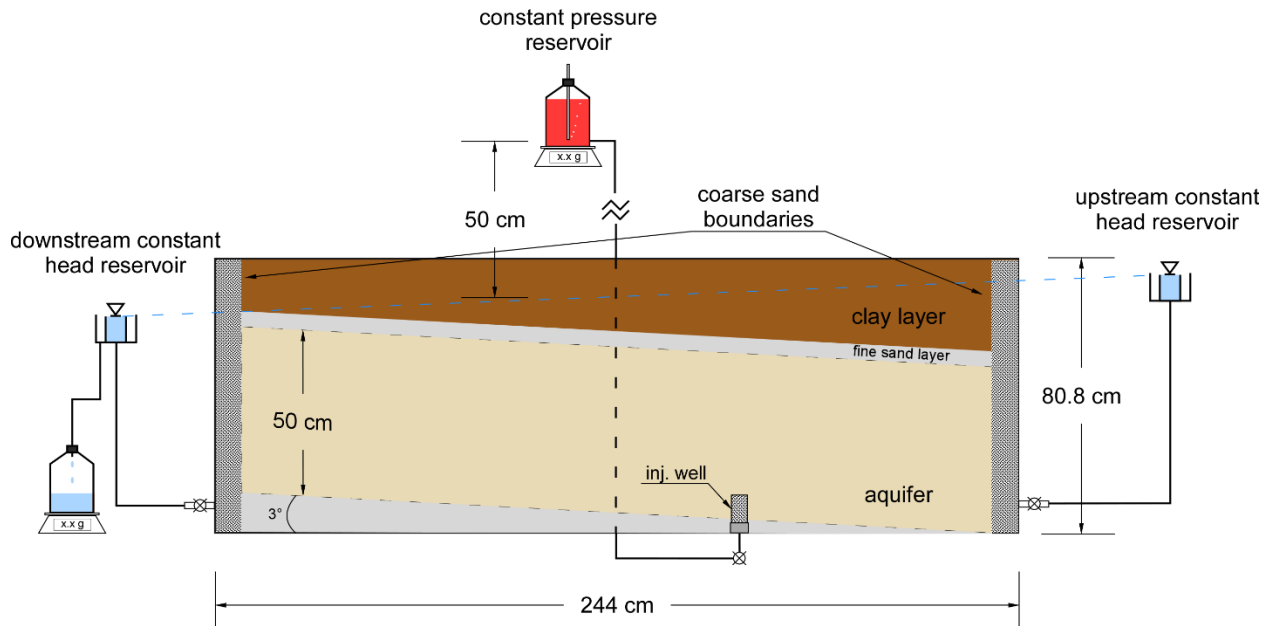
138 <sup>b</sup> measurement from *Bennion and Bachu* [2006], T = 43°C, P = 20 MPa, brine salinity = 2.7% wt.

139 <sup>c</sup> estimates from *Singh et al.* [2010] for Sleipner field

## 140 2.2 Experimental aquifer tank

141 Both homogeneous and heterogeneous scenarios are performed in a sand pack enclosed by a  
142 Plexiglas and aluminum tank with internal dimensions (L × W × H) of (244 × 5 × 80.8) cm<sup>3</sup>. Each  
143 experiment consists of four stages: two NWP injection events separated by as many fluid  
144 redistribution (gravity relaxation) stages, during which the plume is allowed to reach hydrostatic  
145 equilibrium. Figure 1 illustrates the geometry of the tank setup and the sand arrangement for the  
146 homogeneous configuration (#50 sand for the aquifer, #8 sand for injection well and boundary  
147 layers, a fine sand mixture for the bottom and top aquitards, and a clay layer as caprock). The  
148 aquifer has a 5% slope (3° dip angle) achieved by tilting the setup during packing and a constant  
149 background WP flow is maintained in the updip direction by two constant head reservoirs  
150 connected to the coarse sand boundaries. The injection well consists of a 10-cm-high acrylic pipe  
151 (internal diameter, I.D.=4.5 cm) filled with #8 sand. The well is open at the top and supplied with  
152 NWP through the bottom from a constant pressure reservoir (a Mariotte's bottle) sitting on an  
153 electronic scale at 50 cm above the potentiometric surface. Since this is an inclined surface, the  
154 height difference is calculated with respect to the center of the tank. This pressure-controlled  
155 injection method was adopted for its easy implementation. However, as it will be shown in the

156 Discussion section, the injection flowrate resulting from this constant pressure potential condition  
 157 shows fluctuations due to the influence of 1) the relative permeability of the NWP and 2) the  
 158 intrinsic permeability of the sands intersected by the plume.



159  
 160 **Figure 1** Schematic of the flow cell. Injection of NWP takes place from a well placed at the  
 161 bottom of the aquifer. The aquifer has a gentle slope ( $3^\circ$ ) in the direction of the ambient flow  
 162 (right to left). Coarse #8 sand is packed along upstream and downstream boundaries to equally  
 163 constrain constant head conditions. Electronic scales continuously track NWP inflow and WP  
 164 outflow masses.

### 165 2.3 Design of the heterogeneous setup

166 To explicitly represent a sedimentary structure with a correlated permeability field in a  
 167 synthetic aquifer we follow the experimental approaches of *Barth et al.* [2001] and *Fernandez-*  
 168 *Garcia et al.* [2004]. Six different sieve sizes are used to approximate a target log-normal  
 169 distribution of the facies-based permeability field and populate a two-dimensional rectangular  
 170 array of 122 by 25 cells with dimensions  $(2 \times 2) \text{ cm}^2$ . The six categories (or facies) correspond to  
 171 Granusil silica sands #16, #20, #30, #50, #70, and #110, from coarsest to finest, spatially arranged

172 as shown in Figure 2A (see Table 2 for physical properties of the sands). Figure 2B shows the  
 173 target histogram of  $\ln k$  values for the six facies populating the permeability field (except for #8  
 174 sand used for boundaries and wells). Their volumetric fractions are: 3%, 11.4%, 19.5%, 30.8%,  
 175 24.6%, and 10.7%, respectively, following the log-normal distribution of permeability. The  
 176 moderate permeability contrast of the experimental setup is used to shorten the experimental time  
 177 by facilitating faster plume migration compared to actual reservoirs.

178 In order to compare the degree of heterogeneity of the synthetic reservoir with cases of  
 179 practical interest, we estimate the permeability variation using the Dykstra-Parson coefficient  $V_{DP}$   
 180 [Craig, 1993]:

$$181 \quad V_{DP} = \frac{k_{50} - k_{84.1}}{k_{50}} = 1 - e^{-\sigma} \quad (1)$$

182 where  $k_{50}$  is the mean permeability and  $k_{84.1}$  is the mean permeability plus one standard deviation;  
 183 for a homogeneous reservoir  $V_{DP}$  approaches zero, while for an extremely heterogeneous reservoir  
 184  $V_{DP}$  would approach one. For this study,  $V_{DP}$  is 0.73, which is in agreement with values reported  
 185 in the literature [Behzadi and Alvarado, 2012; Farajzadeh et al., 2011; Kumar et al., 2005;  
 186 Saadatpoor et al., 2010; Tchelepi and Orr, 1994; Tian et al., 2016]. Another metric often  
 187 considered is the variance of  $\ln k$  ( $\sigma^2_{\ln k}$ ). In this study, a variance of 1.69 is selected, falling in the  
 188 range of values (0.2 to 5) reported by a number of modeling studies relevant to GCS [Cameron  
 189 and Durlofsky, 2012; Deng et al., 2012; Flett et al., 2004; Han et al., 2010; Lengler et al., 2010].

190 Capillary pressure  $P_c(S)$  drainage curves of the sands cover a range of capillary entry pressures  
 191 between 0.28 kPa and 2.04 kPa (Figure 2C). These values define the ability of NWP to invade a  
 192 given sand, while the final saturation in each sand is controlled by the so-called buoyancy pressure,

193  $P_b$ , exerted by the height difference  $H$  between the injected NWP and the resident WP during the  
194 injection (50 cm).

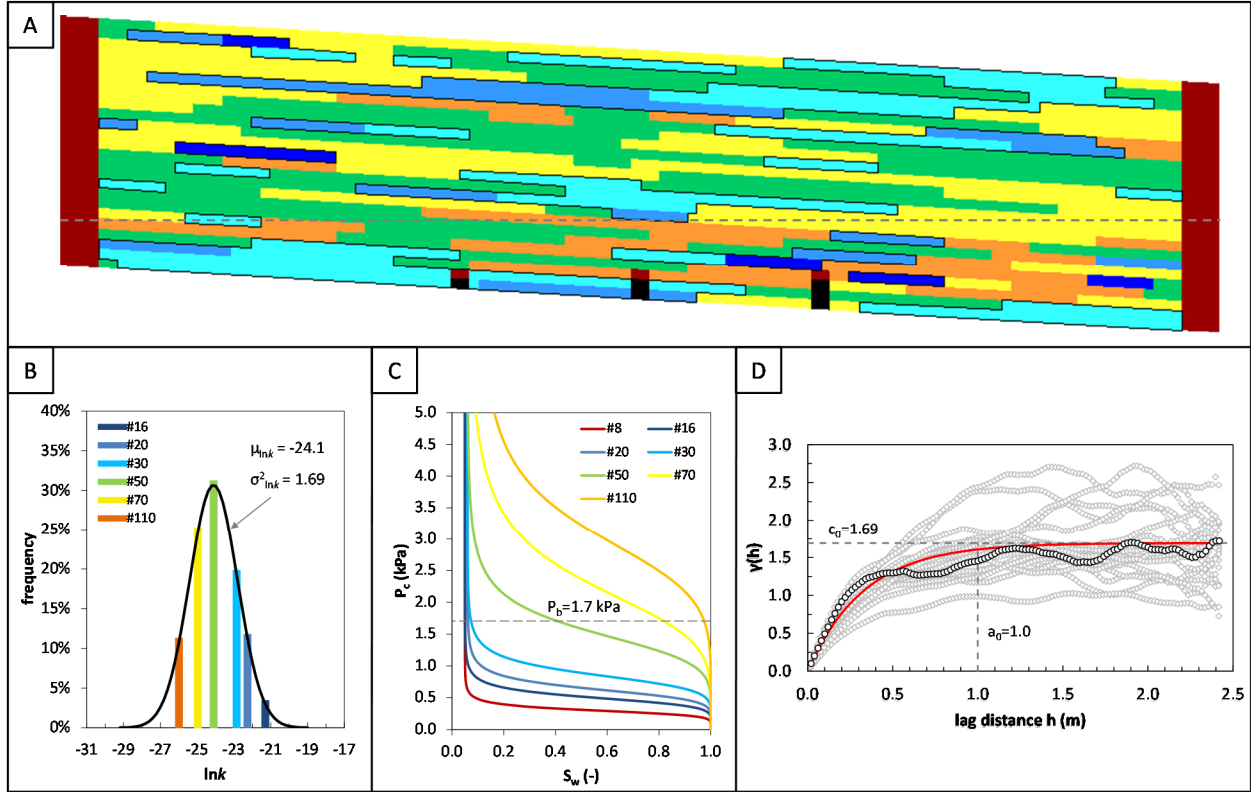
$$195 \quad P_b = (\rho_w - \rho_{nw})gH \quad (2)$$

196 where  $\rho_w$  and  $\rho_{nw}$  are the densities of WP and NWP, respectively, and  $g$  is the gravitational constant.  
197 For simplicity, equation 2 defines  $P_b$  at the injection point, where it takes a value of 1.7 kPa, which  
198 is estimated using  $H=50$  cm. Since this in an open system, as the plume moves upwards, this initial  
199 buoyancy pressure will dissipate proportionally to its vertical location.

200 The spatial sand distribution is designed to mimic a layered structure that recreates a  
201 permeability field in agreement with most reservoir simulations [e.g., *Deng et al.*, 2012; *Flett et*  
202 *al.*, 2007; *Han et al.*, 2010; *Saadatpoor et al.*, 2010; *Tian et al.*, 2016]. The Sequential Indicator  
203 Simulation (SIS) algorithm [*Journel and Alabert*, 1990] combined with the open source program  
204 SGeMS [*Remy et al.*, 2009] is used to generate 20 equiprobable realizations based on an  
205 exponential variogram (equation 3).

$$206 \quad \gamma(h_i) = c_0 \left[ 1 - \exp\left(-\frac{3h_i}{a_{0,i}}\right) \right] \quad (3)$$

207 where  $c_0$  is the sill,  $h_i$  is the lag distance in the  $i$  direction ( $x, z$ ), and  $a_{0,i}$  is the range. The correlation  
208 length is defined as  $\lambda_i = a_{0,i}/3$ . The layered structure is built by assigning long horizontal (100/3  
209 cm) and shorter vertical (4/3 cm) correlation lengths as input parameters for SIS simulations.  
210 Figure 2D shows the experimental variograms along the flow direction for 20 SIS realizations  
211 (gray symbols), highlighting the theoretical variogram (red line) and realization #18 (black  
212 symbols).



213  
214  
215  
216  
217  
218  
219

**Figure 2** A) spatial arrangement of the six sand categories in SIS realization #18, with highlighted high- $k$  clusters (dashed line represents x-ray detection edge); B) target histograms for the six sands representing a  $\ln k$  distribution ( $k$  in  $\text{m}^2$ ); C) characteristic  $P_c(S)$  drainage curve for each sand, including #8 sand used for lateral boundaries and wells; D) theoretical (red line) and experimental (symbols) variograms for 20 realizations of the permeability field; the black variogram represents the realization selected for the packing setup (#18).

220  
221

**Table 2** Physical properties of the silica sand grades used in the experiments from *Sakaki and Illangasekare [2007]*.

Material ID	Sieve size	$k$ ( $\text{m}^2$ )	$\ln k$	$\phi_{avg}$ (-)	$d_{50}$ (mm)	$d_{60}/d_{10}$ (-)
1	#16	$5.62 \times 10^{-10}$	-21.3	0.397	0.88	1.72
2	#20	$2.14 \times 10^{-10}$	-22.3	0.41	0.7	
3	#30	$1.23 \times 10^{-10}$	-22.8	0.433	0.5	1.50
4	#50	$3.37 \times 10^{-11}$	-24.1	0.4	0.3	1.94
5	#70	$1.43 \times 10^{-11}$	-25.0	0.44	0.2	1.86
6	#110	$5.21 \times 10^{-12}$	-26.0	0.38	0.12	~2.0

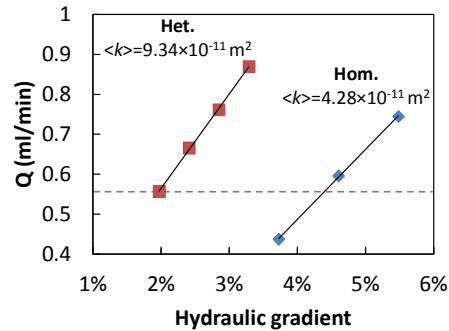
222 Prior to injection, the porosity variation of the sand pack was determined for both  
223 homogeneous and heterogeneous packing configurations by measuring x-ray attenuation across  
224 the flow domain (supporting information Figure S1). Since the sands have all similar porosity  
225 (~0.4), their spatial distribution is not distinguishable from this contour plot; however, the evidence  
226 of an inclined stratification, as well as of the clay layer confining the aquifer (porosity>0.5) is  
227 clear. The higher average porosity observed in the heterogeneous case is due to the looser packing  
228 carried out to minimize the mixing of finer and coarser sands.

## 229 **2.4 Boundary conditions**

230 A constant pressure ( $P_b=1.7$  kPa) boundary condition is applied at the injection well (see Figure  
231 1). The target volume for each injection is 1 L, corresponding to approximately 0.044 pore volumes  
232 (estimated using extents of the aquifer multiplied by average porosity;  $229\text{ cm} \times 5\text{ cm} \times 50\text{ cm} \times$   
233  $0.4$ ). Interestingly, despite both experiments share the same injected volume, the injections exhibit  
234 variable flowrate and therefore different duration. This behavior is further discussed in Section  
235 4.3.

236 Prior to NWP injection, different background hydraulic gradients were tested to mimic the  
237 effect of regional groundwater flow through deep saline aquifers [*Larkin, 2010*], as shown in  
238 Figure 3. For the heterogeneous scenario, a 4.5-cm head difference across the domain was selected,  
239 resulting in a WP flow discharge of 0.56 ml/min at the left boundary and corresponding to a 2%  
240 hydraulic gradient. The latter was increased to 4.5% in the homogeneous scenario to maintain a  
241 similar WP flow discharge. This comparison shows the direct manifestation of the presence of  
242 high permeability layers channeling the flow in the heterogeneous setting, as the estimated

243 effective permeability for the heterogeneous case is  $9.34 \times 10^{-11} \text{ m}^2$  and twice of the permeability  
244 for the homogeneous case ( $4.28 \times 10^{-11} \text{ m}^2$ ).



245  
246 **Figure 3** Correlation between background hydraulic gradient and outflow rate  $Q$  (dashed line  
247 represents the 0.56 ml/min wetting phase flow discharge applied to both experiments).

## 248 2.5 Successive drainage and imbibition experiments

249 For each sand-packed large tank (homogeneous or heterogeneous), the experiment includes  
250 the first injection event with a target NWP volume of 1L, the first redistribution (or imbibition)  
251 event with no injection, the second injection event with the same volume, and the second  
252 redistribution event. Each of the redistribution events stops when no further movement of the  
253 plume is observed along horizontal and vertical directions. The design of these experiments aims  
254 to assess long-term migration and trapping of NWP in the meter-scale system. To the best  
255 knowledge of the authors, the long-term m-scale experiments conducted in this study are the first  
256 of the kind, providing a necessary dataset for understanding field-scale processes of  $\text{scCO}_2$   
257 migration and trapping. The reservoir thickness used in this study is only one order of magnitude  
258 smaller than that for some pilot and demonstration GCS projects. For example, the Frio C sand  
259 used for  $\text{CO}_2$  injection in the Frio pilot test is  $\sim 5$  meter thick.

260 Central to the experimental approach is the use of x-ray attenuation to measure the spatial and  
261 temporal distribution of the phase saturations in the sand pack non-invasively and with high spatial  
262 resolution (one measure every 15 mm in x and z directions). The saturation measurements  
263 represent a depth-average along the second horizontal axis (y) and an areal average over a sampling  
264 volume determined by the radius of the collimated x-ray beam (1 mm). Further details about the  
265 x-ray attenuation device, both hardware- and software-wise, as well as the procedure for x-ray data  
266 conversion into actual phase path-lengths can be found in *Trevisan et al.* [2014] and *Trevisan*  
267 [2015]. In conjunction with x-ray attenuation measurements, photographic images of the  
268 transparent walls of the flow cell are continuously gathered in order to discard any preferential  
269 flow of NWP along the vertical walls.

### 270 **3. Experimental results**

271 To show the effect of known heterogeneity structures on migration and trapping of NWP fluid,  
272 we present experimental observations for both homogeneous and heterogeneous setups in a similar  
273 fashion. Figure 4 and Figure 5 illustrate the development of NWP plumes qualitatively, with  
274 photography, and quantitatively, with saturation contours gathered via x-ray attenuation, for these  
275 experiments. For the sake of conciseness, only plume snapshots acquired at the end of the injection  
276 and redistribution stages are presented, while a more complete set of results at additional times is  
277 available as supplementary materials (Figure S.I.1 and Figure S.I.2). The tables embedded in  
278 Figure 4 and Figure 5 summarize the NWP mass balance corresponding to each snapshot. The  
279 NWP volumes are broken down into inflow, outflow, detected plume (above  $z=0$ ), and undetected  
280 plume (below  $z=0$ ) volumes within the sandbox. As a comparative measure between the two  
281 scenarios, we introduce a trapping efficiency factor,  $\varepsilon = V_{plume}/V_{inflow}$ , to represent the fraction



282 of NWP (detected and undetected) that remains in the domain with respect to the total amount  
283 injected. Additionally, we introduce the perimeter-to-area ratio ( $P/A$ ) as an indicator of plume  
284 surface available for dissolution and chemical reactions.

### 285 **3.1 Homogeneous scenario**

286 The homogeneous experiment is designed to represent the simplest setting for a buoyant plume  
287 to migrate through a porous domain. The purpose of this fairly simplistic setup is twofold: 1) to  
288 observe plume behavior during successive drainage and imbibition events, which could be used in  
289 the future for testing two-phase flow models considering the effect of hysteresis, and 2) to provide  
290 a control experiment to compare with a more complex permeability field. To facilitate the  
291 comparison between both scenarios, we analyze each of the four stages separately.

292 *First Injection Stage* (0 to 22.05 hours, Figure 4, top row): early evolution of the plume appears  
293 to be controlled by buoyancy force, showing a chimney-like structure, which gradually develops  
294 into an asymmetrical shape, driven by the background WP flow from right to left. Since the plume  
295 reaches the caprock at the same time the injection is halted, the influence of aquifer dip on plume  
296 geometry is minimal during this stage. Also, towards the completion of this stage, the displacement  
297 front shows some unstable behavior characterized by several short-range fingers, possibly due to  
298 the buildup of the injection flow rate, causing viscous forces to dominate over capillary forces.  
299 The plume at the end of this stage is referred to “early plume”, and the saturation (i.e., maximum  
300 initial saturation for later imbibition) in this plume under drainage is relatively high.

301 *First Fluid Redistribution Stage* (22.05 to 327.27 hours, Figure 4, second row): once the first  
302 injection is complete, the plume is allowed to redistribute until it approaches equilibrium, which  
303 is considered when no further movement of the plume is observed along horizontal and vertical

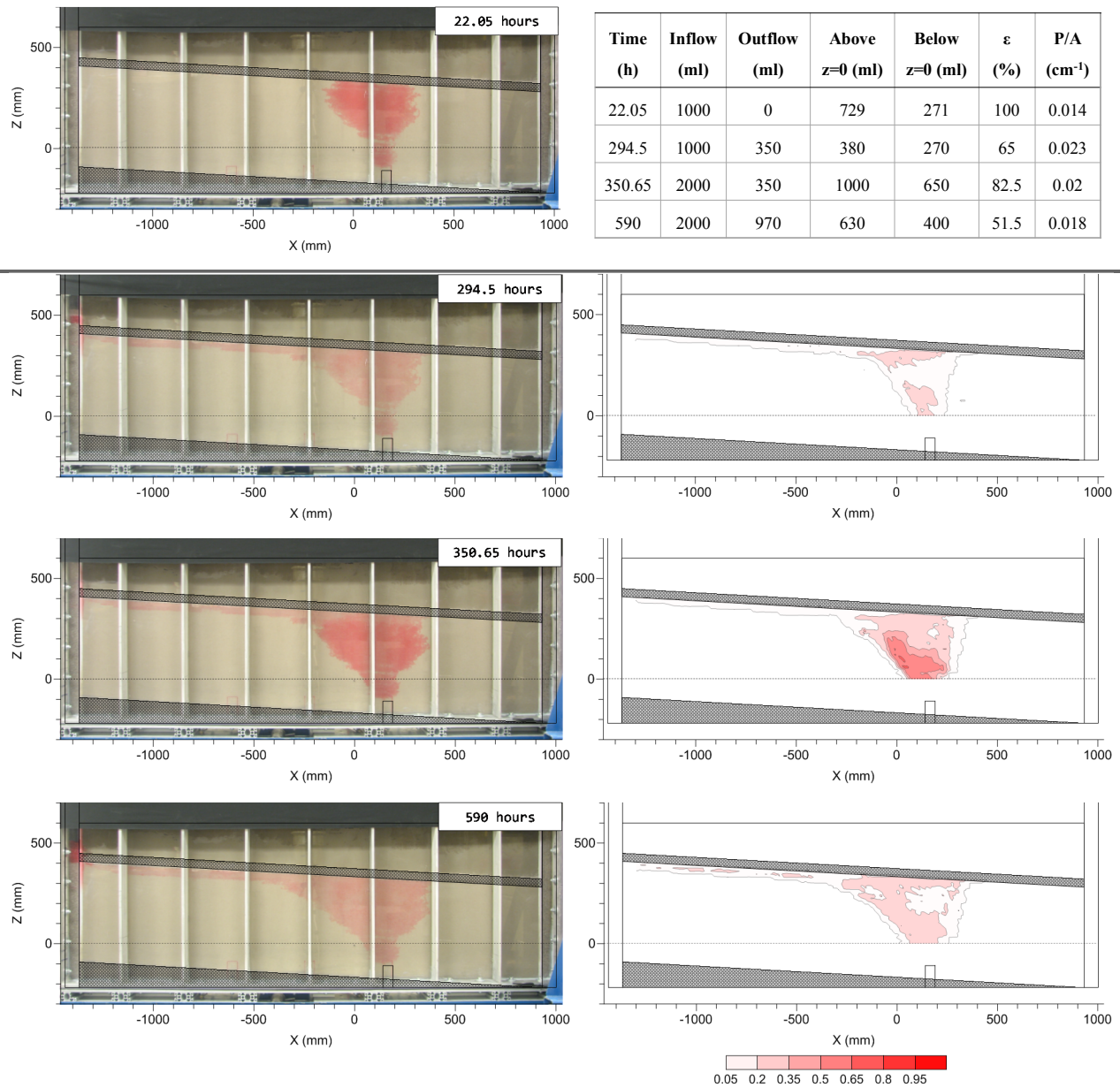
304 directions (as shown in the Discussion section). During this buoyancy-dominated relaxation  
305 process, the plume (i.e., the post-injection plume) develops predominantly along a thin layer  
306 underneath the caprock and leaves behind a trail of residual saturation. Approximately 11 days  
307 after the injection ends, 35% of the injected mass has escaped out of the aquifer and the post-  
308 injection plume takes an average NWP saturation of 17%. Interestingly, this residually-trapped  
309 saturation is not homogeneously distributed within the plume, as shown by the x-ray contour maps,  
310 where values range between 5% and 20%. The highest saturation of trapped NWP occurs in the  
311 footprint of the early plume event and can be attributed to the high initial saturation within this  
312 footprint. Out of this footprint, the post-injection plume experiences drainage and imbibition  
313 during the redistribution period, and has much smaller initial maximum saturation (than that in the  
314 early plume at the end of the first injection event) that results in even smaller saturation of trapped  
315 NWP. These results indicate that the observed behavior of trapped NWP may be represented by  
316 existing empirical [e.g., *Land*, 1968] or non-empirical trapping models [e.g., *Cihan et al.*, 2014;  
317 *Cihan et al.*, under review]. The irregular saturation distribution within the footprint of the early  
318 plume probably results from the imperfect nature of the sand packing causing water encroachment  
319 to occur by non-uniform displacement/imbibition, as shown in pore network experiments by  
320 *Chang et al.* [2016]. Although the behavior observed here has been predicted at the reservoir scale  
321 by several continuum-based multiphase flow models [*Flett et al.*, 2007; *Kumar et al.*, 2005;  
322 *Lengler et al.*, 2010], no experimental evidence has been yet reported with such detailed  
323 characterization of the saturation distribution.

324 *Second Injection Stage* (327.27 to 350.65 hours, Figure 4, third row): during early times of the  
325 second injection event, the plume follows the path established by the previous injection event.  
326 However, before the target injection volume is reached, the lateral spreading of the plume increases

327 resulting in a wider footprint than the early plume, as well as larger median plume saturation (0.46  
328 vs. 0.38), as shown in Figure 7. The larger spreading and higher saturation are most likely due to  
329 1) the presence of trapped NWP in the early plume that has a detrimental effect on relative WP  
330 permeability as compared to the nearby NWP-free regions, 2) right-to-left background WP flow  
331 that results in the skewness of the plume, and 3) the dynamic evolution with additional injection  
332 that would occur for the same continuously injected volume of 2 L. All these effects cannot be  
333 distinguished by the only one dataset without comparison.

334 *Second Fluid Redistribution Stage* (350.65 to 590 hours, Figure 4, bottom row): the positive  
335 impact of a second injection event is revealed by the area occupied by the plume after the 2<sup>nd</sup>  
336 redistribution, which is 23% larger than the area occupied after the 1<sup>st</sup> injection and redistribution.  
337 Consequently, a larger footprint enables a 58% increase in residually stored mass. On the other  
338 hand, this experiment shows the principal disadvantage of fairly homogeneous and isotropic  
339 reservoirs, where gravity segregation causes the plume to bypass a large fraction of the reservoir.  
340 From the NWP saturation contour maps obtained with x-ray attenuation, a concave region of lower  
341 saturation surrounded by relatively higher saturation can be observed, as a possible effect of the  
342 background WP flow on plume trapping. Similar effects on the inhomogeneity of the trapped  
343 saturation distribution as for the first redistribution, but the region with higher residual saturations  
344 seems to be larger.

345 Note that the plume is always continuous in its footprint at the different stages of the  
346 experiment. The trapping efficiency factor after the second redistribution stage is 51.5%, smaller  
347 than 65% after the end of the first redistribution stage. However, a NWP volume of 1030 ml is  
348 trapped within a wider plume, larger than the total trapped volume of 650 ml after the first  
349 redistribution stage.



350 Figure 4 Homogeneous base case experiment: plume snapshots taken via photography (left) and  
 351 x-ray attenuation (right) at the end of each stage: 1<sup>st</sup> injection (1<sup>st</sup> row), 1<sup>st</sup> redistribution (2<sup>nd</sup>  
 352 row), 2<sup>nd</sup> injection (3<sup>rd</sup> row), and 2<sup>nd</sup> redistribution (4<sup>th</sup> row). Total NWP volumes corresponding  
 353 to each snapshot are listed in the table.

### 354 3.2 Heterogeneous scenario

355 *First Injection Stage* (0 to 27.3 hours, Figure 5, top row): as opposed to the homogenous  
 356 scenario, where the plume freely migrates upward and reaches the caprock by the end of the first

357 injection event, the presence of capillary and permeability barriers of finer sands in the  
358 heterogeneous scenario leads to a considerable reduction in vertical migration distance. The  
359 injected NWP fluid migrates into a cluster of connected coarse sands (#16, #20, #30) that is  
360 immediately above the injection well and bounded by fine #110 sand from the left and right sides  
361 and by #70 sand from the top of the cluster (see Figure 2A). With time, the injected NWP fluid  
362 accumulates in this high-permeability cluster, pools under the overlying less permeable #70 sand,  
363 and migrates downward to the left side following the structure of the coarse sands. This results in  
364 an increase in plume thickness and thus NWP pressure at the top of this NWP pool. When the  
365 NWP pressure at the bottom of #70 sand is higher than its entry capillary pressure ( $\sim 1.2$  kPa), the  
366 capillary barrier is broken and NWP starts to migrate upward through the #70 sand into the second  
367 cluster of coarse sands to form the second pool of NWP. Clearly, the plume includes two separate  
368 pools connected by a flow path through #70 sand where NWP saturation is small. However, it is  
369 this low-saturation flow path that supplies all NWP mass in the second, upper pool. The second  
370 cluster consists of #30 sand and #16 sand to the left and is bounded from the top by a continuous  
371 layer of #70 sand crossing over the entire sandbox length. At the end of this stage, the second pool  
372 is filled by NWP only in the #30 sand portion of this cluster. This accumulation-penetration-  
373 breakthrough phenomenon was simulated for stratified intra-formation layers for the Illinois Basin  
374 [Birkholzer and Zhou, 2009; Zhou et al., 2010], but this phenomenon is shown the first time in a  
375 laboratory experiment with sufficient aquifer thickness.

376 *First Fluid Redistribution Stage* (27.3 to 262.42 hours, Figure 5, second row): at the end of  
377 this stage, all injected NWP mass is trapped within the two pools by capillary barriers of the  
378 surrounding finer sands and local residual saturation in the two clusters of coarse sands. With time,  
379 the first, lower pool shrinks a little bit and its saturation decreases, leading to the reduction in NWP

380 pressure at the top of the pool. The reduced NWP mass from the lower pool migrates through the  
381 #70 sand flow path into the second, upper pool. At the end of this stage, the flow through this path  
382 ceases because at the bottom of this path, the continuous reduction in the NWP pressure and  
383 saturation leads to the balance between capillary force of the finer sand and buoyancy force from  
384 the lower pool. The capillary barrier of the fine #70 sand is recovered from its broken condition,  
385 trapping large amount of NWP mass in the lower pool with higher saturation than local residual  
386 saturation (~20%). With continuous inflow from the lower pool and redistribution in the upper  
387 pool, NWP fluid migrates updip to the left side and fills in a new branch of #16 sand facies. At the  
388 end of this stage, the saturation distribution in the upper pool follows the balance between capillary  
389 and buoyancy forces at any location of the pool. Due to the updip feature of the cluster and the  
390 pool, buoyancy-induced NWP pressure is the highest at the upper end of the pool on the left and  
391 lowest on the lower end of the pool on the right, resulting in the saturation variability in the pool.

392 The entire upper pool is trapped by the capillary barrier of the overlying continuous #70 sand  
393 layer, as the highest NWP pressure at the upper-left end of the pool is still lower than the entry  
394 capillary pressure of #70 sand. The upper pool is also surrounded by finer #50 sand on its left side  
395 and #50 and #70 sands on the right side of the pool. This phenomenon of a NWP pool of high  
396 saturation trapped in a “pocket-shaped” cluster of high-permeability sands by surrounding lower-  
397 permeability sands or shales on all sides (at least top and updip) except one in-flow side is referred  
398 to as “pocket” trapping. The in-flow side can be the downdip or bottom side through which NWP  
399 fluid or scCO<sub>2</sub> is supplied. The pocket trapping is caused by capillary and permeability barrier  
400 effects along the semi-closed boundary of the trapped NWP pool. This trapping is similar to the  
401 dead-end effect in contaminant transport [*Coats and Smith, 1964*] and hydrocarbon trapping in  
402 anticlines.

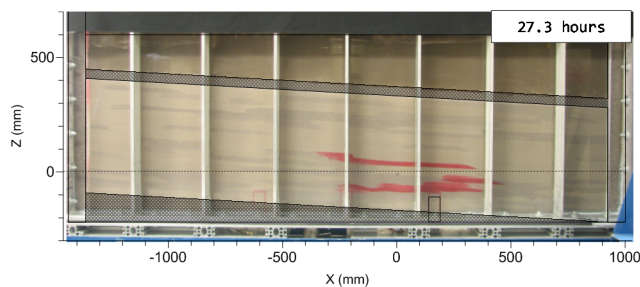
403        *Second Injection Stage* (262.42 to 293.42 hours, Figure 5, third row): the lower cluster of  
404 coarse sands and the lower NWP pool is additionally charged by injected NWP fluid, leading to  
405 an increase in NWP saturation in this pool. The increased saturation leads to higher capillary  
406 pressure at the top of the pool and the bottom of inter-pool #70 sand, breaking the capillary barrier  
407 again. Once the inter-pool flow path is reactivated for flow, the NWP pressure at the top of the  
408 upper pool increases sharply because the entire plume (i.e., the two pools and the inter-pool flow  
409 path) is connected, leading to much higher NWP columns. This higher NWP pressure drives NWP  
410 upward migration into the #50 sand facies overlying the #30 sand in the downdip portion and  
411 overlying the #16 sand in the updip portion of the upper pool.

412        *Second Fluid Redistribution Stage* (293.42 to 2400 hours, Figure 5, bottom row): with time of  
413 redistribution, NWP migrates updip further in the #50 sand from the #16 branch to expand the  
414 second pool. Meanwhile, the NWP pressure is sufficiently high at the updip ends of the pool, and  
415 thus breaks the capillary barrier of the continuous #70 sand layer at two locations. The newly-  
416 created two flow paths through #70 sand facilitate upward migration of NWP to form the third  
417 pool in the third cluster of #20, 30, and #50 sand. The same accumulation-penetration-  
418 breakthrough process continues to create the fourth and the fifth NWP pool. The fifth pool is  
419 connected to the left-side boundary, resulting in outflow of 35.7% of the injected mass from the  
420 sandbox. .

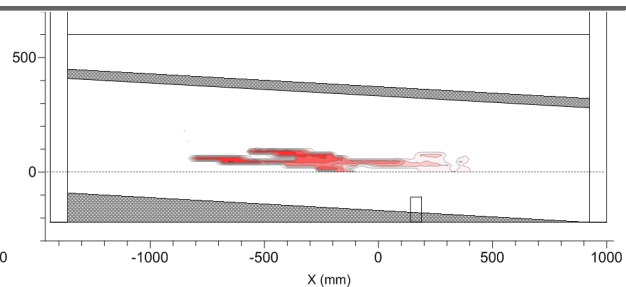
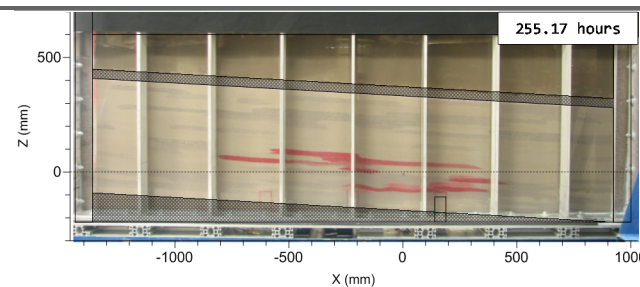
421        This last stage takes 2.9 months to reach quasi-hydrostatic equilibrium. 64.3% of the injected  
422 NWP is immobilized within the aquifer, a 12.8% increase with respect to the homogeneous  
423 scenario. Another significant feature of the plume is its specific surface area, represented by the  
424 P/A ratio, showing a tenfold increase with respect to the end of the first redistribution stage, and a

425 37-fold increase with respect to the end of the second redistribution stage for the homogeneous  
 426 scenario.

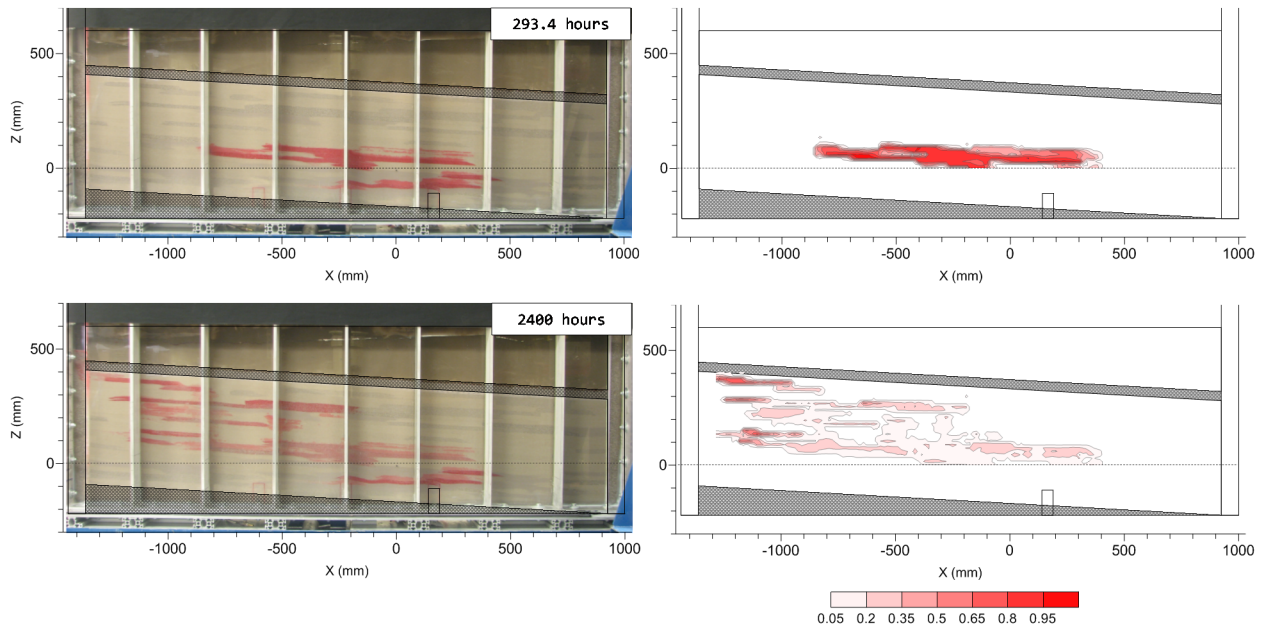
427 Note that the contrasts of permeability and entry capillary pressure among the six sand facies  
 428 are chosen to show all the physical processes and phenomena, including pooling under finer facies  
 429 and capillary barrier effect, breakthrough of capillary barriers caused by buoyancy-enhanced NWP  
 430 pressure, start and cessation of inter-pool NWP flow, and cyclic drainage and imbibition. These  
 431 contrasts are also chosen to show residual trapping, hysteresis caused by cyclic drainage and  
 432 imbibition, and pocket trapping that mainly depends on the heterogeneity structures. These chosen  
 433 contrasts make this unique experiment feasible at the time scale of 100 days and the spatial scale  
 434 of 244 cm × 80.8 cm × 5 cm. The physical processes and phenomena and the trapping mechanisms  
 435 demonstrated in the experiment are relevant to the field-scale GCS reservoirs that have much  
 436 higher contrasts of permeability and entry capillary pressure. The higher contrasts will facilitate  
 437 some phenomena, such as pocket trapping.



Time (h)	Inflow (ml)	Outflow (ml)	Above z=0 (ml)	Below z=0 (ml)	$\epsilon$ (%)	P/A ( $\text{cm}^{-1}$ )
27.3	1000	0	353	647	100	0.082
255.17	1000	0	601	399	100	0.082
293.4	2000	0	1250	750	100	0.062
2400	2000	714	900	386	64.3	0.672







438 **Figure 5** Heterogeneous experiment: plume snapshots taken via photography (left) and x-ray  
 439 attenuation (right) at the end of each stage: 1<sup>st</sup> injection (1<sup>st</sup> row), 1<sup>st</sup> redistribution (2<sup>nd</sup> row), 2<sup>nd</sup>  
 440 injection (3<sup>rd</sup> row), and 2<sup>nd</sup> redistribution (4<sup>th</sup> row). Total NWP volumes corresponding to each  
 441 snapshot are listed in the table.

#### 442 4. Discussion

443 Some important observations made in the homogeneous experiment include: 1) the linear  
 444 increase in injection flowrate with time under the constant injection pressure condition, and the  
 445 subsequent development of displacement front instabilities, 2) the absence of remobilized NWP  
 446 during the second injection and the larger footprint achieved afterwards, and 3) the non-uniform  
 447 NWP saturation distribution within the early plume footprint. The heterogeneous experiment  
 448 provides the following observations: 1) the absence of CO<sub>2</sub> outflow after the first fluid  
 449 redistribution, and 2) the longer time of plume redistribution (2.8 months). Some of these  
 450 observations in the two experiments cannot be predicted by the state-of-the-art mathematical  
 451 models, thus offering an opportunity to improve these models.

## 452 4.1 Spatial moment analysis

453 Besides visual observations and quantitative measurement of plume saturation via x-ray  
454 attenuation, we assess the spreading of the plume throughout the various stages of the experiments  
455 via analysis of spatial moments [Eichel *et al.*, 2005; Fagerlund *et al.*, 2007; Han *et al.*, 2010;  
456 Kueper and Frind, 1991]. For an immiscible plume, the zeroth moment,  $M_{000}$ , is defined in a  
457 similar manner as for a solute concentration [Freyberg, 1986]:

$$458 \quad M_{000}(t) = \sum_i \varphi^i(x, y, z) S_{NW}^i(x, y, z, t) V^i \quad (4)$$

459 where  $\varphi^i$  is the porosity (space-dependent) and  $S_{NW}^i$  is the space- and time-dependent NWP  
460 saturation for the  $i^{\text{th}}$  gridblock with volume  $V^i$ . The first moments in the x- and z-direction  
461 normalized by the total NWP volume present in the domain ( $M_{000}$ ) define the coordinates of the  
462 plume centroid:

$$463 \quad x_c(t) = \frac{M_{100}}{M_{000}} = \frac{\sum_i x^i \varphi^i(x, y, z) S_{NW}^i(x, y, z, t) V^i}{\sum_i \varphi^i(x, y, z) S_{NW}^i(x, y, z, t) V^i} \quad (5)$$

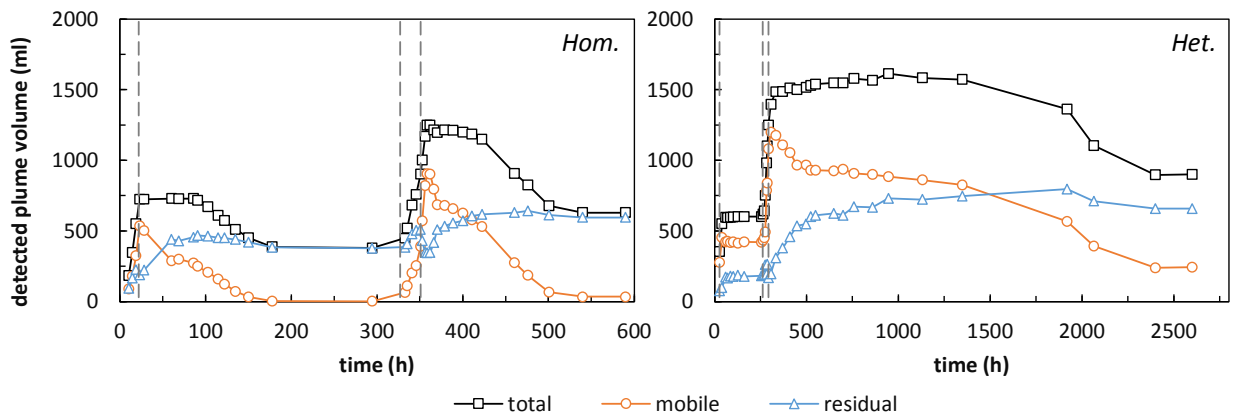
$$464 \quad z_c(t) = \frac{M_{001}}{M_{000}} = \frac{\sum_i z^i \varphi^i(x, y, z) S_{NW}^i(x, y, z, t) V^i}{\sum_i \varphi^i(x, y, z) S_{NW}^i(x, y, z, t) V^i} \quad (6)$$

### 465 4.1.1 Zeroth moment

466 A critical problem related to the long-term containment of CO<sub>2</sub> in deep reservoirs and recently  
467 tackled by tracer tests is the assessment of the amount that is being retained under residual  
468 saturation conditions [LaForce *et al.*, 2014; Myers *et al.*, 2015; Rasmusson *et al.*, 2014]. In fact,  
469 any part of the plume occurring at saturations higher than residual is considered mobile and  
470 susceptible to further displacement, unless additional trapping mechanisms, such as dissolution  
471 trapping and pocket trapping, get underway. The controlled laboratory experiments in conjunction  
472 with a refined x-ray scanning grid allow for accurate quantification of the total NWP volume

473 present in the tank using zeroth moment calculations. To evaluate the effects of capillary barriers  
 474 and sequential injections on the retention of NWP we selected a cut-off value of 0.22 to  
 475 differentiate mobile and residual fractions of a saturation at local scale. This cut-off value  
 476 represents the maximum residual NWP saturation of the homogeneous experiment; however, this  
 477 cut-off value is higher than actual residual saturation values owing to the hysteretic behavior of  
 478 the  $P_c(S)$  relationship [Cihan *et al.*, under review], and may result in slight over-prediction of the  
 479 immobile volume and under-prediction of the mobile volume.

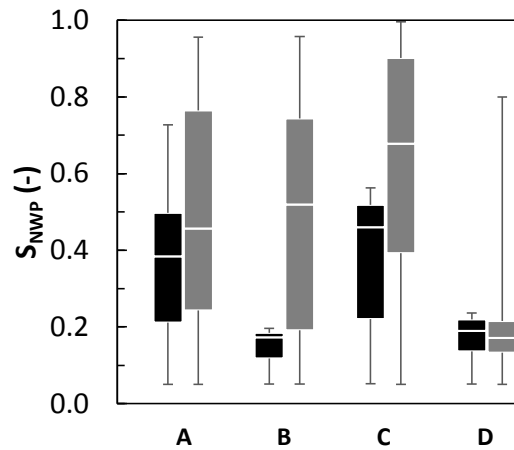
480 As shown in Figure 6, both experiments reach an apparent hydrostatic equilibrium at the end  
 481 of the experiments as no further changes in the trapped NWP mass (mobile and immobile) are  
 482 observed. The final residually-trapped volumes are similar for the homogeneous and  
 483 heterogeneous cases, 595 ml and 657 ml, respectively. However, the final mobile volume (243  
 484 ml) in the heterogeneous case is significantly larger than that (34 ml) in the homogeneous case,  
 485 because of local structural “pocket” trapping caused by heterogeneity structures and capillary  
 486 barrier effects. In addition, the heterogeneity elongates the time (3.6 months) needed for plume  
 487 stabilization after two injection events, much longer than that (24 days) for the homogeneous cases.



488

489 **Figure 6** Zeroth moment evolution representing total plume volume (detected by x-ray scanning)  
490 during both experiments (black squares). Orange circles and blue triangles differentiate mobile  
491 and residual portions of the plume, respectively. Dashed lines delineate the two injection events.

492 Additionally to the analysis of total plume volume, assessing the range of NWP saturations  
493 measured at the end of each stage provides information about the trapping capacity of each  
494 scenario (Figure 7). At the end of both injection stages (stages A and C), capillary barriers have a  
495 dominant effect on plume migration in the heterogeneous scenario, leading to the highest  
496 saturations after the second injection. After the first fluid redistribution (stage B), the mobile NWP  
497 fluid exists over 70% of the plume footprint under pocket trapping in the heterogeneous case, while  
498 a residual (immobile) saturation state has been reached in 99% of the plume footprint in the  
499 homogeneous case. Finally, at the experiment completion (stage D), the main difference in terms  
500 of saturation distribution between both scenarios is the presence, although scattered, of high  
501 saturation areas in the heterogeneous case.

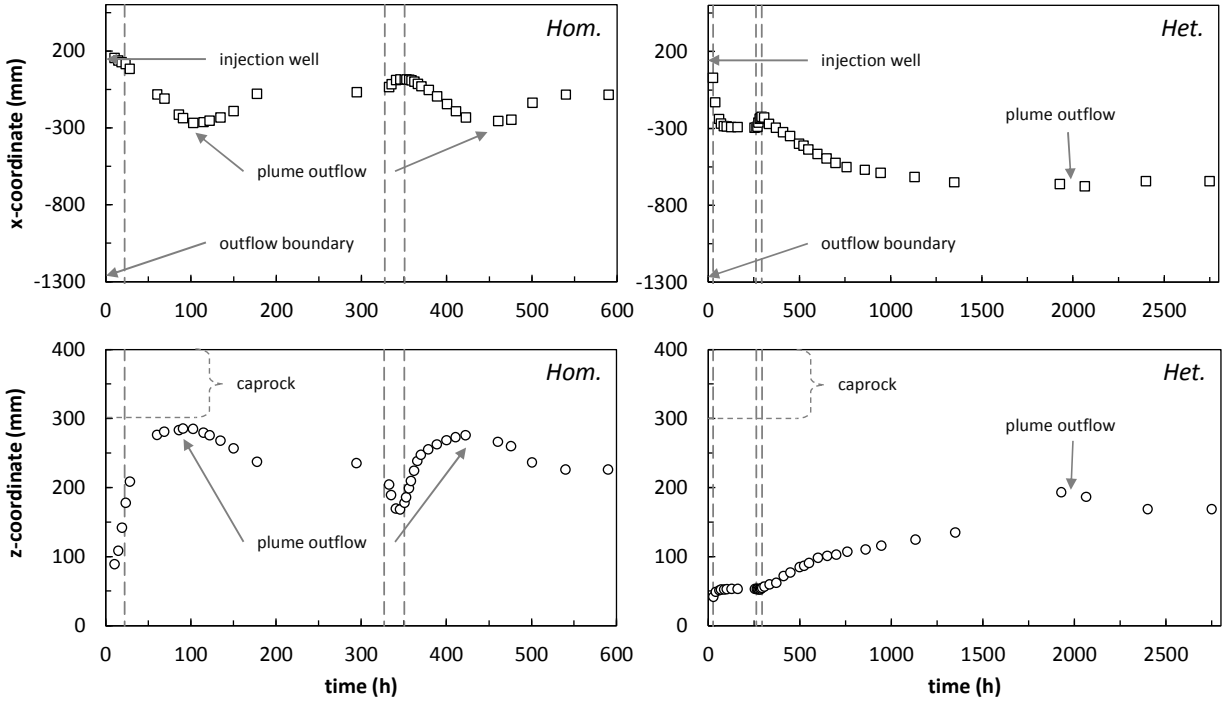


502 **Figure 7** NWP saturation distributions measured at the end of each stage for both experiments  
503 (black for homogeneous, gray for heterogeneous). A) end of 1<sup>st</sup> injection; B) end of 1<sup>st</sup>  
504 redistribution; C) end of 2<sup>nd</sup> injection; D) end of 2<sup>nd</sup> redistribution.  
505

#### 506 4.1.2 First moment

507 The analysis of first spatial moments allows tracking the position of plume's centroid in the x-  
508 z plane during the temporal evolution of the NWP plume. As shown in Figure 8, whenever the  
509 plume breaks through at the outflow boundary, the center of mass reverses its original migration  
510 direction (both horizontally and vertically) and starts moving countercurrent with respect to the  
511 dipping angle of the aquifer and the background flow. This characteristic behavior is observed in  
512 both scenarios and during both injection events. In the homogeneous scenario, the observed  
513 behavior is essentially identical during the two injection events. In the heterogeneous scenario  
514 (right column in Figure 8), however, an overall equilibrium is quickly attained after the first  
515 injection, both horizontally and vertically, while after the second injection event, a slower upward,  
516 left-bound movement of the plume centroid takes place for approximately two months,  
517 culminating with the breakthrough into the outflow boundary.

518 Another interesting observation is that in the homogeneous scenario the plume remains very  
519 close to the caprock, as compared to the heterogeneous scenario. This behavior could have  
520 important implications in actual field conditions, where avoiding a prolonged seal exposure to CO<sub>2</sub>  
521 may prevent mineral reaction that can undermine its geological integrity.



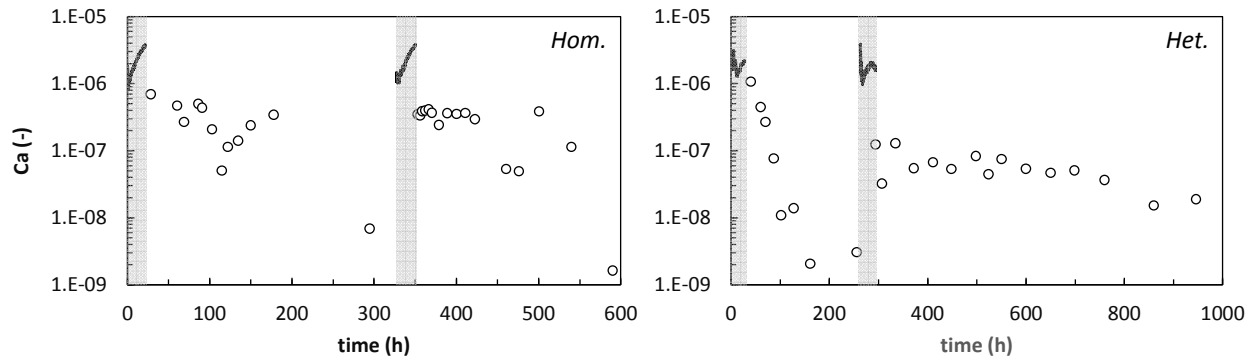
522

523 **Figure 8** Temporal evolution of the horizontal (squares, top row) and vertical (circles, bottom  
 524 row) coordinates of the plume center of mass during both experiments. The intervals shown by  
 525 the vertical dashed lines represent the duration of the injection events. X-coordinates decrease  
 526 towards the left (outflow) boundary of the domain. Z-coordinates of caprock vary from 300 mm  
 527 (right boundary) to 400 mm (left boundary).

528 **4.2 Assessment of flow regimes**

529 As the primary objective of this type of experiments is to mimic flow behavior of a  $\text{scCO}_2$   
 530 plume through a brine-saturated aquifer, the injection flowrate was maintained inside the limits of  
 531 capillary/buoyancy-dominated flow regime. Evidence from laboratory [England *et al.*, 1987] and  
 532 field observations [Cavanagh and Haszeldine, 2014] suggest that for capillary number ( $\text{Ca}$ )  $< 10^{-5}$ ,  
 533 buoyant fluids such as oil or  $\text{CO}_2$  move across the porous medium via gravity-driven ganglia  
 534 and therefore can be modeled with numerical methods that neglect viscous forces, such as invasion  
 535 percolation [Frette *et al.*, 1992; Meckel *et al.*, 2015]. For the experiments presented here we  
 536 estimate capillary numbers with two different methods: 1) from NWP velocity (flowrate/well area)

537 during the injection and 2) from plume's center of mass velocity (length/time) during the fluid  
 538 redistribution stages. The evolution of the capillary number presented in Figure 9 points toward  
 539 similar injection flow regimes for both experiments and higher influence of capillary forces  
 540 (smaller Ca) during gravity relaxation for the heterogeneous scenario.



541  
 542 **Figure 9** Evolution of the capillary number during homogeneous (left) and heterogeneous (right)  
 543 experiments. Calculations of NWP velocity are based on injection flowrate (continuous lines)  
 544 and average displacement of plume centroid (circles). Shaded areas represent injection periods.  
 545 For visualization purposes, the length of the heterogeneous plot was reduced from 2500 to 1000  
 546 hours.

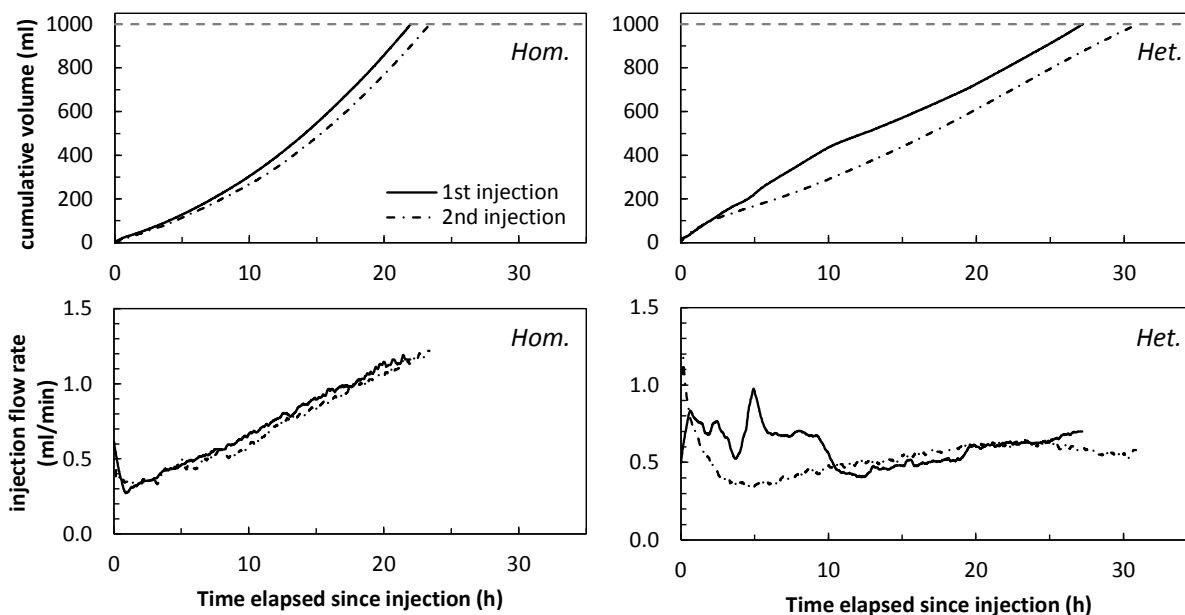
### 547 4.3 Injection flow rate evolution

548 For the homogeneous experiment (Figure 10, left column), the first and second injection events  
 549 take 22 hours and 23 hours to complete the target injection volume of 1 L. For both injection  
 550 events, the flow rate rose monotonically from 0.31 ml/min to 1.16 ml/min. This behavior could be  
 551 explained by near-well enhanced NWP relative permeability caused by saturation increase with  
 552 time and by the growth of the plume in both length and width.

553 For the heterogeneous experiment (Figure 10, right column), the injection duration extends to  
 554 27 and 30 hours during the first and second injection events. During the first injection, the flow  
 555 rate shows several rapid changes indicating a strong influence of the permeability structure. The  
 556 higher rate during the first 10 hours indicates easy injection into the first cluster of high-

557 permeability sand facies (see Figure 2A) with the lower plume pool as shown in the first row of  
558 Figure 5. The later behavior of the injection rate with a decrease and then a gradual increase  
559 indicates the impact of low-permeability sand (#70) that is broken through by NWP to form the  
560 upper plume pool. The smaller fluctuations of the injection rate show the impacts of smaller-scale  
561 structures of permeability within each cluster. For the second injection event, the injection rate  
562 decreases sharply and then increases gradually, showing a smoother evolution. This behavior of  
563 the injection rate clearly shows the control of the low-permeability sand between the two clusters  
564 of high-permeability sands. The quick reduction can be attributed to this structure because the high  
565 saturation in the lower pool remains stable during the first redistribution stage and thus does not  
566 change the relative permeability significantly. At later time of injection, the rate is similar for both  
567 injection events because the flow paths connecting the two pools are also stable in terms of  
568 saturation and relative permeability. Overall, the evolution of the injection rate depends on the  
569 absolute permeability, saturation-dependent relative permeability and the structure of absolute  
570 permeability that controls the pools of plume. It will be very interesting to use numerical modeling  
571 to match the observed flow rates with all known heterogeneity structures and plume evolution with  
572 quantified high-resolution saturation.





573  
 574 **Figure 10** Evolution of cumulative inflow volume (top row) and flow rate (bottom row) of  
 575 Soltrol 220 for the homogeneous (left column) and heterogeneous (right column) experiment.  
 576 Target injected volume (1000 ml for each injection event) is highlighted by horizontal dashed  
 577 lines for cumulative volumes.

#### 578 4.4 Comparison with small-tank experiments

579 The immiscible displacement experiments, referred to as large tank experiments, performed in  
 580 the 2.4 m × 0.5 m sandbox represent the last iteration of the experimental analysis on capillary  
 581 trapping that originated from smaller (0.7 m × 0.16 m) and less complex setups [Trevisan *et al.*,  
 582 2015; Trevisan *et al.*, 2014]. With respect to previous small tank experiments, the progression to  
 583 the current large tank system involves four main additional features: 1) a larger influence of  
 584 buoyancy forces, enabled by a lower aspect ratio of the aquifer; 2) the implementation of a  
 585 background hydraulic gradient; 3) the sequential injection scheme and cyclic drainage and  
 586 imbibition; 4) a larger variability of the permeability field. These features, in addition to the meter-  
 587 scale system and long-term monitoring, make some of the observations discussed above unique  
 588 and first of the kind.

## 589 5. Concluding remarks

590 The large tank experiments show the asymptotic values of trapping and storage efficiency  
591 factors with multiple cycles of drainage and imbibition under an ideal homogeneous scenario and  
592 a more realistic heterogeneous one. The trapping efficiency factor reduces from 65% after the first  
593 redistribution stage to 51.5% after the second redistribution stage in the homogeneous experiment,  
594 while it reduces from 100% to 64.3% from the first to the second redistribution stage in the  
595 heterogeneous experiment. The enhanced trapping efficiency in the heterogeneous case can be  
596 attributed to the local structural trapping, i.e., pocket trapping, which is caused by combined  
597 heterogeneity structure and capillary barrier effect. For the homogeneous case, all trapped NWP  
598 mass is due to combined residual saturation and hysteresis caused by cyclic drainage and  
599 imbibition. Even though the beneficial effects of sequential injections cannot be fully tested due  
600 to unfeasibility to perform a benchmark experiment with one single 2L-injection, such schemes  
601 are being increasingly scrutinized and often advocated by numerical studies [*Huber et al.*, 2016;  
602 *Rasmusson et al.*, 2016; *Shamshiri and Jafarpour*, 2012].

603 The observations of these large tank sandbox experiments allow to draw the following  
604 conclusions:

- 605 1. When performed in relatively homogeneous systems, subsequent NWP injections can enhance  
606 the reservoir space occupied by the plume, increase NWP mass trapped by capillary forces,  
607 and achieve higher residual saturations by hysteresis caused by drainage/imbibition cycles.  
608 Under constant injection pressure, the injection rate for the two injection events linearly  
609 increases with time following the same trend.

610 2. For the heterogeneous case, injected NWP accumulates in clusters of high-permeability sand  
611 facies to form plume pools of with higher saturation trapped under the capillary barrier effect  
612 in addition to hysteresis and residual saturation. Connecting these separate plume pools are  
613 low-permeability sand facies through which NWP has to break under buoyancy to achieve high  
614 storage and trapping efficiency.

615 3. The constant NWP injection pressure in the heterogeneous case results in fluctuations in the  
616 injection rate, reflecting the effect of permeability structure, the evolution of plume clusters,  
617 and NWP migration through low-permeability facies that connecting these pools. This  
618 observation can be relevant to field situations where formation injectivity can show significant  
619 variations in time.

620 4. Layer-type heterogeneity exerts a major control on the migration and trapping of the plume,  
621 leading to longer displacement times to reach stable trapping conditions, dampened vertical  
622 migration, and immobilization of larger fraction of injected mass within coarser sand zones.

623 The outcomes presented in this study highlight the convenience of sandbox experiments for  
624 mimicking a realistic aquifer configuration and interplay of governing forces. As part of the  
625 continuing effort to improve numerical predictions of storage capacity and efficiency, these  
626 surrogate systems are instrumental to identify the relevant migration and trapping phenomena that  
627 need to be considered by mathematical models. For instance, given their capillary-dominated flow  
628 regime, these experiments lend themselves to benchmark the performance of existing and new  
629 two-phase flow simulators.

630        **Acknowledgements**

631        Funding for this research is provided by the U.S. Department of Energy through the National  
632 Energy Technology Laboratory's CO<sub>2</sub> sequestration R&D Program under grant DE-FE0004630  
633 and National Science Foundation Award no. EAR-1045282 through the Hydrologic Sciences  
634 Program. Supporting information is included as three Figures in an S.I. file and as one Excel  
635 spreadsheet; any additional data may be obtained from Luca Trevisan (email:  
636 [luca.trevisan@gmail.com](mailto:luca.trevisan@gmail.com)). LT thanks Tip Meckel and Susan Hovorka for insightful discussions  
637 and acknowledges additional funding from the Bureau of Economic Geology.

- 639 Agartan, E., L. Trevisan, A. Cihan, J. Birkholzer, Q. Zhou, and T. H. Illangasekare (2015),  
640 Experimental study on effects of geologic heterogeneity in enhancing dissolution trapping of  
641 supercritical CO<sub>2</sub>, *Water Resour Res*, 51(3), 1635-1648.
- 642 Barth, G. R., T. H. Illangasekare, and H. Rajaram (2003), The effect of entrapped nonaqueous  
643 phase liquids on tracer transport in heterogeneous porous media: laboratory experiments at the  
644 intermediate scale, *J Contam Hydrol*, 67(1-4), 247-268.
- 645 Barth, G. R., M. C. Hill, T. H. Illangasekare, and H. Rajaram (2001), Predictive modeling of  
646 flow and transport in a two-dimensional intermediate-scale, heterogeneous porous medium,  
647 *Water Resour Res*, 37(10), 2503-2512.
- 648 Behzadi, H., and V. Alvarado (2012), Upscaling of upward CO<sub>2</sub> migration in 2D system, *Adv*  
649 *Water Resour*, 46, 46-54.
- 650 Bennion, D. B., and S. Bachu (2006), Dependence on Temperature, Pressure, and Salinity of the  
651 IFT and Relative Permeability Displacement Characteristics of CO<sub>2</sub> Injected in Deep Saline  
652 Aquifers, in *2006 SPE Annual Technical Conference and Exhibition*, edited, Society of  
653 Petroleum Engineers, San Antonio, Texas, U.S.A.
- 654 Birkholzer, J. T., and Q. Zhou (2009), Basin-scale hydrogeologic impacts of CO<sub>2</sub> storage:  
655 Regulatory and capacity implications, *International Journal of Greenhouse Gas Control* 3 (6),  
656 745–756.
- 657 Bryant, S. L., S. Lakshminarasimhan, and G. A. Pope (2008), Buoyancy-Dominated Multiphase  
658 Flow and Its Effect on Geological Sequestration of CO<sub>2</sub>, *Spe J.*, 13(4), 447-454.
- 659 Buscheck, T. A., Y. Sun, M. Chen, Y. Hao, T. J. Wolery, W. L. Bourcier, B. Court, M. A. Celia,  
660 S. J. Friedmann, and R. D. Aines (2012), Active CO<sub>2</sub> reservoir management for carbon storage:  
661 Analysis of operational strategies to relieve pressure buildup and improve injectivity,  
662 *International Journal of Greenhouse Gas Control*, 6, 230-245.
- 663 Cameron, D. A., and L. J. Durlofsky (2012), Optimization of well placement, CO<sub>2</sub> injection  
664 rates, and brine cycling for geological carbon sequestration, *International Journal of Greenhouse*  
665 *Gas Control*, 10, 100-112.
- 666 Cavanagh, A. J., and R. S. Haszeldine (2014), The Sleipner storage site: Capillary flow modeling  
667 of a layered CO<sub>2</sub> plume requires fractured shale barriers within the Utsira Formation,  
668 *International Journal of Greenhouse Gas Control*, 21, 101-112.
- 669 Chang, C., Q. Zhou, T. J. Kneafsey, M. Oostrom, T. W. Wietsma, and Q. Yu (2016), Pore-scale  
670 supercritical CO<sub>2</sub> dissolution and mass transfer under imbibition conditions, *Adv Water Resour*,  
671 92, 142-158.

- 672 Cihan, A., J. T. Birkholzer, and M. Bianchi (2015), Optimal well placement and brine extraction  
673 for pressure management during CO<sub>2</sub> sequestration, *International Journal of Greenhouse Gas*  
674 *Control*, 42, 175-187.
- 675 Cihan, A., J. T. Birkholzer, L. Trevisan, A. Gonzalez-Nicolas, and T. H. Illangasekare (under  
676 review), Investigation of representing hysteresis in macroscopic models of two-phase flow in  
677 porous media using intermeditate scale experimental data.
- 678 Cinar, Y., A. Riaz, and H. A. Tchelepi (2009), Experimental Study of CO<sub>2</sub> Injection Into Saline  
679 Formations, *Spe J.*, 14(4), 588-594.
- 680 Coats, K. H. & Smith, B. D. (1964) Dead-end pore volume and dispersion in porous media. SPE  
681 Journal 4(1), 73–84, doi:0.2118/647-PA.
- 682 Craig, F. F. (1993), *The reservoir engineering aspects of waterflooding*, 134 p. pp., Henry L.  
683 Doherty Memorial Fund of AIME, Richardson, Tex.
- 684 Deng, H. L., P. H. Stauffer, Z. X. Dai, Z. S. Jiao, and R. C. Surdam (2012), Simulation of  
685 industrial-scale CO<sub>2</sub> storage: Multi-scale heterogeneity and its impacts on storage capacity,  
686 injectivity and leakage, *International Journal of Greenhouse Gas Control*, 10, 397-418.
- 687 Doughty, C., and K. Pruess (2004), Modeling supercritical carbon dioxide injection in  
688 heterogeneous porous media, *Vadose Zone J*, 3(3), 837-847.
- 689 Eichel, H., R. Helmig, I. Neuweiler, and O. A. Cirpka (2005), Upscaling of Two-Phase Flow  
690 Processes in Porous Media, in *Upscaling Multiphase Flow in Porous Media: From Pore to Core*  
691 *and Beyond*, edited by D. B. Das and S. M. Hassanizadeh, pp. 237-257, Springer Netherlands.
- 692 England, W. A., A. S. Mackenzie, D. M. Mann, and T. M. Quigley (1987), The Movement and  
693 Entrapment of Petroleum Fluids in the Subsurface, *J Geol Soc London*, 144, 327-347.
- 694 Fagerlund, F., T. H. Illangasekare, and A. Niemi (2007), Nonaqueous-phase liquid infiltration  
695 and immobilization in heterogeneous media: 1. Experimental methods and two-layered reference  
696 case, *Vadose Zone J*, 6(3), 471-482.
- 697 Farajzadeh, R., P. Ranganathan, P. L. J. Zitha, and J. Bruining (2011), The effect of  
698 heterogeneity on the character of density-driven natural convection of CO<sub>2</sub> overlying a brine  
699 layer, *Adv Water Resour*, 34(3), 327-339.
- 700 Fernandez-Garcia, D., T. H. Illangasekare, and H. Rajaram (2004), Conservative and sorptive  
701 forced-gradient and uniform flow tracer tests in a three-dimensional laboratory test aquifer,  
702 *Water Resour Res*, 40(10).
- 703 Flett, M., R. Gurton, and I. Taggart (2004), The Function of Gas-Water Relative Permeability  
704 Hysteresis in the Sequestration of Carbon Dioxide in Saline Formations, in *SPE Asia Pacific Oil*  
705 *and Gas Conference and Exhibition*, edited, Society of Petroleum Engineers, Perth, Australia.

706 Flett, M., R. Gurton, and G. Weir (2007), Heterogeneous saline formations for carbon dioxide  
707 disposal: Impact of varying heterogeneity on containment and trapping, *J Petrol Sci Eng*, 57(1-  
708 2), 106-118.

709 Frette, V., J. Feder, T. Jossang, and P. Meakin (1992), Buoyancy-Driven Fluid Migration in  
710 Porous-Media, *Phys Rev Lett*, 68(21), 3164-3167.

711 Freyberg, D. L. (1986), A Natural Gradient Experiment on Solute Transport in a Sand Aquifer  
712 .2. Spatial Moments and the Advection and Dispersion of Nonreactive Tracers, *Water Resour*  
713 *Res*, 22(13), 2031-2046.

714 Gasda, S. E., M. A. Celia, and J. M. Nordbotten (2008), Upslope plume migration and  
715 implications for geological CO<sub>2</sub> sequestration in deep, saline aquifers, *The IES Journal Part A:*  
716 *Civil & Structural Engineering*, 1(1), 2-16.

717 Gershenson, N. I., R. W. Ritzi, D. F. Dominic, M. Soltanian, E. Mehnert, and R. T. Okwen  
718 (2015), Influence of small-scale fluvial architecture on CO<sub>2</sub> trapping processes in deep brine  
719 reservoirs, *Water Resour Res*, 51(10), 8240-8256.

720 Glass, R. J., S. H. Conrad, and W. Peplinski (2000), Gravity-destabilized nonwetting phase  
721 invasion in macroheterogeneous porous media: Experimental observations of invasion dynamics  
722 and scale analysis, *Water Resour Res*, 36(11), 3121-3137.

723 Goater, A. L., B. Bijeljic, and M. J. Blunt (2013), Dipping open aquifers—The effect of top-  
724 surface topography and heterogeneity on CO<sub>2</sub> storage efficiency, *International Journal of*  
725 *Greenhouse Gas Control*, 17, 318-331.

726 Gonzalez-Nicolas, A., L. Trevisan, T. H. Illangasekare, A. Cihan, and J. T. Birkholzer (under  
727 review), Enhancing trapping effectiveness through proper time scheduling of injection of  
728 supercritical CO<sub>2</sub> in heterogeneous formations.

729 Gunn, I., and A. W. Woods (2011), On the flow of buoyant fluid injected into a confined,  
730 inclined aquifer, *J Fluid Mech*, 672, 109-129.

731 Han, W. S., S. Y. Lee, C. A. Lu, and B. J. McPherson (2010), Effects of permeability on CO<sub>2</sub>  
732 trapping mechanisms and buoyancy-driven CO<sub>2</sub> migration in saline formations, *Water Resour*  
733 *Res*, 46, W07510.

734 Hesse, M., H. A. Tchelepi, and F. M. Orr (2006), Scaling Analysis of the Migration of CO<sub>2</sub> in  
735 Saline Aquifers.

736 Huber, E. J., A. D. Stroock, and D. L. Koch (2016), Analysis of a time dependent injection  
737 strategy to accelerate the residual trapping of sequestered CO<sub>2</sub> in the geologic subsurface,  
738 *International Journal of Greenhouse Gas Control*, 44, 185-198.

739 Ide, S. T., K. Jessen, and F. M. Orr (2007), Storage of CO<sub>2</sub> in saline aquifers: Effects of gravity,  
740 viscous, and capillary forces on amount and timing of trapping, *International Journal of*  
741 *Greenhouse Gas Control*, 1(4), 481-491.

- 742 Journal, A. G., and F. Alabert (1990), New Method for Reservoir Mapping, *J Petrol Technol*,  
743 42(2).
- 744 Kopp, A., H. Class, and R. Helmig (2009), Investigations on CO<sub>2</sub> storage capacity in saline  
745 aquifers-Part 2: Estimation of storage capacity coefficients, *International Journal of Greenhouse*  
746 *Gas Control*, 3(3), 277-287.
- 747 Kueper, B. H., and E. O. Frind (1991), Two-phase flow in heterogeneous porous media: 2.  
748 Model application, *Water Resour Res*, 27(6), 1059-1070.
- 749 Kumar, A., M. Noh, G. A. Pope, K. Sepehrnoori, S. Bryant, and L. W. Lake (2005), Reservoir  
750 Simulation of CO<sub>2</sub> Storage in Deep Saline Aquifers, *Spe J.*, 10(3), 336-348.
- 751 Kuo, C. W., and S. M. Benson (2015), Numerical and analytical study of effects of small scale  
752 heterogeneity on CO<sub>2</sub>/brine multiphase flow system in horizontal corefloods, *Adv Water Resour*,  
753 79, 1-17.
- 754 LaForce, T., J. Ennis-King, C. Boreham, and L. Paterson (2014), Residual CO<sub>2</sub> saturation  
755 estimate using noble gas tracers in a single-well field test: The CO<sub>2</sub>CRC Otway project,  
756 *International Journal of Greenhouse Gas Control*, 26, 9-21.
- 757 Land, C. (1968), Calculation of Imbibition Relative Permeability for Two- and Three-Phase  
758 Flow From Rock Properties, *Spe J.*, 8(2), 149-156.
- 759 Larkin, R. (2010), Hydrodynamic Trapping of CO<sub>2</sub> Geosequestered in Saline Aquifers, in *SPE*  
760 *Improved Oil Recovery Symposium*, edited, Tulsa, Oklahoma, USA.
- 761 Lengler, U., M. De Lucia, and M. Kuhn (2010), The impact of heterogeneity on the distribution  
762 of CO<sub>2</sub>: Numerical simulation of CO<sub>2</sub> storage at Ketzin, *International Journal of Greenhouse*  
763 *Gas Control*, 4(6), 1016-1025.
- 764 Li, B. X., and S. M. Benson (2015), Influence of small-scale heterogeneity on upward CO<sub>2</sub>  
765 plume migration in storage aquifers, *Adv Water Resour*, 83, 389-404.
- 766 MacMinn, C. W., M. L. Szulczewski, and R. Juanes (2010), CO<sub>2</sub> migration in saline aquifers.  
767 Part 1. Capillary trapping under slope and groundwater flow, *J Fluid Mech*, 662, 329-351.
- 768 Meckel, T. A., S. L. Bryant, and P. R. Ganesh (2015), Characterization and prediction of CO<sub>2</sub>  
769 saturation resulting from modeling buoyant fluid migration in 2D heterogeneous geologic  
770 fabrics, *International Journal of Greenhouse Gas Control*, 34, 85-96.
- 771 Mikes, D., and J. Bruining (2006), Standard flow cells to incorporate small-scale heterogeneity  
772 (crossbedding) in a reservoir model, *Mar Petrol Geol*, 23(9-10), 979-993.
- 773 Myers, M., L. Stalker, T. La Force, B. Pejčić, C. Dyt, K.-B. Ho, and J. Ennis-King (2015), Field  
774 measurement of residual carbon dioxide saturation using reactive ester tracers, *Chem Geol*, 399,  
775 20-29.



- 776 Neufeld, J. A., M. A. Hesse, A. Riaz, M. A. Hallworth, H. A. Tchelepi, and H. E. Huppert  
777 (2010), Convective dissolution of carbon dioxide in saline aquifers, *Geophys Res Lett*, 37.
- 778 Nordbotten, J. M., M. A. Celia, and S. Bachu (2005), Injection and storage of CO<sub>2</sub> in deep saline  
779 aquifers: Analytical solution for CO<sub>2</sub> plume evolution during injection, *Transp. Porous Media*,  
780 58(3), 339-360.
- 781 Pickup, G., P. S. Ringrose, and A. Sharif (2000), Steady-State Upscaling: From Lamina-Scale to  
782 Full-Field Model, *Spe J.*, 5(2).
- 783 Pini, R., Krevor, S. C., & Benson, S. M. (2012), Capillary pressure and heterogeneity for the  
784 CO<sub>2</sub>/water system in sandstone rocks at reservoir conditions. *Advances in Water Resources*, 38,  
785 48-59.
- 786 Polak, S., Y. Cinar, T. Holt, and O. Torsaeter (2015), Use of low- and high-IFT fluid systems in  
787 experimental and numerical modelling of systems that mimic CO<sub>2</sub> storage in deep saline  
788 formations, *J Petrol Sci Eng*, 129, 97-109.
- 789 Rasmusson, K., M. Rasmusson, Y. Tsang, and A. Niemi (2016), A simulation study of the effect  
790 of trapping model, geological heterogeneity and injection strategies on CO<sub>2</sub> trapping,  
791 *International Journal of Greenhouse Gas Control*, 52, 52-72.
- 792 Rasmusson, K., M. Rasmusson, F. Fagerlund, J. Bensabat, Y. Tsang, and A. Niemi (2014),  
793 Analysis of alternative push-pull-test-designs for determining in situ residual trapping of carbon  
794 dioxide, *International Journal of Greenhouse Gas Control*, 27, 155-168.
- 795 Remy, N., A. Boucher, and J. Wu (2009), *Applied geostatistics with SGeMS : a user's guide*, xix,  
796 264 p. pp., Cambridge University Press, Cambridge, UK ; New York.
- 797 Ringrose, P. S., K. S. Sorbie, P. W. M. Corbett, and J. L. Jensen (1993), Immiscible flow  
798 behaviour in laminated and cross-bedded sandstones, *J Petrol Sci Eng*, 9(2), 103-124.
- 799 Ritzi, R. W., J. T. Freiburg, and N. D. Webb (2016), Understanding the (co) variance in  
800 petrophysical properties of CO<sub>2</sub> reservoirs comprising sedimentary architecture, *International*  
801 *Journal of Greenhouse Gas Control*, 51, 423-434.
- 802 Saadatpoor, E., S. L. Bryant, and K. Sepehrnoori (2010), New Trapping Mechanism in Carbon  
803 Sequestration, *Transp. Porous Media*, 82(1), 3-17.
- 804 Sakaki, T., and T. H. Illangasekare (2007), Comparison of height-averaged and point-measured  
805 capillary pressure-saturation relations for sands using a modified Tempe cell, *Water Resour Res*,  
806 43(12).
- 807 Shamshiri, H., and B. Jafarpour (2012), Controlled CO<sub>2</sub> injection into heterogeneous geologic  
808 formations for improved solubility and residual trapping, *Water Resour Res*, 48(2).

809 Singh, V., A. Cavanagh, H. Hansen, B. Nazarian, M. Iding, and P. Ringrose (2010), Reservoir  
810 Modeling of CO<sub>2</sub> Plume Behavior Calibrated Against Monitoring Data From Sleipner, Norway,  
811 in *SPE Annual Technical Conference and Exhibition*, edited, Florence, Italy.

812 Tchelepi, H. A., and F. M. Orr (1994), Interaction of Viscous Fingering, Permeability  
813 Heterogeneity, and Gravity Segregation in Three Dimensions, *SPE Reservoir Engineering*,  
814 9(04), 266-271.

815 Tian, L., Z. Yang, F. Fagerlund, and A. Niemi (2016), Effects of permeability heterogeneity on  
816 CO<sub>2</sub> injectivity and storage efficiency coefficient, *Greenhouse Gases: Science and Technology*,  
817 6(1), 112-124.

818 Trevisan, L. (2015), Study of trapping mechanisms of supercritical carbon dioxide in deep  
819 heterogeneous geological formations through intermediate-scale testing and modeling, PhD  
820 thesis, 189 pp, Colorado School of Mines, Golden, CO.

821 Trevisan, L., P. G. Krishnamurthy, and T. A. Meckel (under review), Impact of 3D capillary  
822 heterogeneity and bedform architecture at the 1 sub-meter scale on CO<sub>2</sub> saturation for buoyant  
823 flow in clastic aquifers.

824 Trevisan, L., R. Pini, A. Cihan, J. T. Birkholzer, Q. Zhou, and T. H. Illangasekare (2015),  
825 Experimental analysis of spatial correlation effects on capillary trapping of supercritical CO<sub>2</sub> at  
826 the intermediate laboratory scale in heterogeneous porous media, *Water Resour Res*, 51(11),  
827 8791-8805.

828 Trevisan, L., A. Cihan, F. Fagerlund, E. Agartan, H. Mori, J. T. Birkholzer, Q. Zhou, and T. H.  
829 Illangasekare (2014), Investigation of mechanisms of supercritical CO<sub>2</sub> trapping in deep saline  
830 reservoirs using surrogate fluids at ambient laboratory conditions, *International Journal of*  
831 *Greenhouse Gas Control*, 29, 35-49.

832 van Lingen, P. P., J. Bruining, and C. P. J. W. van Kruijsdijk (1996), Capillary Entrapment  
833 Caused by Small-Scale Wettability Heterogeneities, *SPE Reservoir Engineering*, 11(02), 93-100.

834 Werner, M., D. Sutter, A. Krattli, O. Lafci, R. Mutschler, P. Oehler, J. Winkler, and M. Mazzotti  
835 (2014), A physical model for geological CO<sub>2</sub> storage - Replacing misconceptions by visual  
836 explanation, *International Journal of Greenhouse Gas Control*, 25, 42-53.

837 Yamamoto, H., K. Zhang, K. Karasaki, A. Marui, H. Uehara, and N. Nishikawa (2009),  
838 Numerical investigation concerning the impact of CO<sub>2</sub> geologic storage on regional groundwater  
839 flow, *International Journal of Greenhouse Gas Control*, 3(5), 586-599.

840 Zhao, B. Z., C. W. MacMinn, H. E. Huppert, and R. Juanes (2014), Capillary pinning and  
841 blunting of immiscible gravity currents in porous media, *Water Resour Res*, 50(9), 7067-7081.

842 Zhou, Q., J. T. Birkholzer, E. Mehnert, Y.-F. Lin, and K. Zhang (2010), Modeling basin- and  
843 plume-scale processes of CO<sub>2</sub> storage for full-scale deployment, *Ground Water*, 48(4), 494-514.

844 Zimoch, P. J., J. A. Neufeld, and D. Vella (2011), Leakage from inclined porous reservoirs, *J*  
845 *Fluid Mech*, 673, 395-405.